Supporting Information

for

Conformation-Dependent Spin Relaxation Behaviors of 6-Oxoverdazyl Radical Single Crystals

Zi-Yuan Wang,[†,‡] Ya-Zhong Dai,[†,‡] Ze-Fan Yao,[†,‡] Bo-Wei Dong,[†] Yang Lu,[†,‡] Li Ding,[†,‡] Shang-Da Jiang,[*,†] Jie-Yu Wang,[*,†,‡] and Jian Pei[*,†,‡]

[†]Beijing National Laboratory for Molecular Sciences (BNLMS), College of Chemistry and Molecular Engineering, Peking University, Beijing 100871, China
[‡]Key Laboratory of Bioorganic Chemistry and Molecular Engineering of Ministry of Education, Center of Soft Matter Science and Engineering, College of Chemistry and Molecular Engineering, Peking University, Beijing 100871, China

Email: jiangsd@pku.edu.cn; jieyuwang@pku.edu.cn; jianpei@pku.edu.cn

General Experimental

All reagents and starting materials were purchased from commercial suppliers and used without further purification. All air and water sensitive reactions were performed under nitrogen atmosphere. Toluene were distilled from sodium prior to use. ^{1}H and ^{13}C NMR spectra were recorded on Bruker ARX-400 (400 MHz). All chemical shifts were reported in parts per million (ppm). ^{1}H NMR chemical shifts were referenced to TMS (0 ppm), and ^{13}C NMR chemical shifts were referenced to CDCl$_3$ (77.00 ppm). Mass spectra were recorded on a Bruker Solarix XR mass spectrometer. Elemental analyses were performed using a German Vario EL III elemental analyzer. Thermal gravity analyses (TGA) were carried out on a TA Instrument Q600 analyzer, and differential scanning calorimetry (DSC) analyses were performed on a METTLER TOLEDO Instrument DSC822 calorimeter. Solution absorption spectra were recorded on PerkinElmer Lambda 750 UV-*vis* spectrometer. Cyclic voltammetry (CV) was performed on BASI Epsilon workstation. Glassy carbon electrode was used as a working electrode and a platinum wire as a counter electrode, and all potentials were recorded versus Ag/AgCl (saturated) as a reference electrode (scan rate: 50 mV s^{-1}). Single-crystal XRD data were collected on an Aglient technologies Super Nova Atlas Dual System with an alternative microfocus source (Mo Kα = 0.71073 Å, Cu Kα = 1.54184 Å) and focusing multilayer mirror optics. The data processing was accomplished with the CrysAlisPro program. The structures were solved by direct methods and refined on F2 anisotropically for all the non-hydrogen atoms by the full-matrix leastsquares method using SHELXL 97 program. Detailed data were listed in Table S2. Powder XRD experiments were performed on a PAN analytical X'Pert PRO diffractometer equipped with a Pixel detector and using Cu Kα source (1.5406 Å). The data were collected under ambient temperature. Mercury 3.8 program was used to simulate the reference patterns based on the crystal structures obtained with single-crystal XRD. EPR spectra were obtained using Bruker E580 X-band variable-temperature apparatus and were simulated with the software of Easyspin. According to the simulated results, such split spectrum could be illustrated by the hyperfine coupling with two nitrogen nuclei and a hydrogen nucleus. Magnetic measurements were performed using a Quantum Design SQUID VSM magnetometer with a field of 0.1 T.

Detailed EPR Measurement Procedure.

The radical molecules were dissolved in a d_8-toluene solution with the concentration of 10^{-4}

mol/L for EPR experiments. Both continuous wave (cw-) and pulse-EPR data were measured on a Bruker Elexsys E580 spectrometer with MS-3 cavity (ω = 9.26 GHz). The low-temperature environment was achieved by Oxford Instruments produced liquid helium cryostats (CF935). The signal of the pulse-EPR experiments was collected by integrating the Hahn echo ($\pi/2$-τ-π-τ-echo) with τ = 200 ns. The T_1 value of B4P-Y was measured by the inversion recovery method (π-T-$\pi/2$-τ-π-τ-echo) with 4-step phase cycling. The T_m value of B4P-Y was obtained by using Hahn echo sequence with 16-step phase cycling. The T_m value of B4P-R was measured by FID detection method ($\pi/2$-FID). The T_1 value of B4P-R was measured by the inversion recovery method (π-T-$\pi/2$-FID). The $\pi/2$ and π pulse lengths in T_1 and T_m measurements were 20 and 40 ns with 6 dB attenuation of the microwave power 300 W, respectively.

Synthesis Details

Compounds **1**, **2**, and **3** were synthesized according to the literature[1,2].
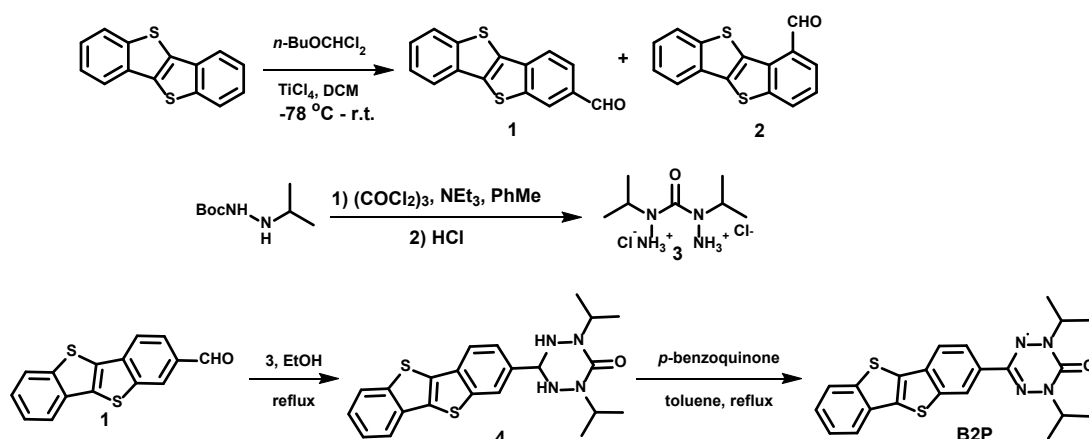
Synthesis of Compound 4. Compound **1** (166 mg, 0.6 mmol) and compound **3** (145 mg, 0.6 mmol) were carefully degassed, then dissolved in 5 mL of ethanol. The mixture was refluxed overnight. After filtration, the residue was washed with ethanol for three times to give pure compound **4** as white powders (167 mg, 63% yield). ^{1}H NMR (400 MHz, CDCl$_3$, ppm): δ 8.17 (s, 1H), 7.93 (dd, J = 15.3, 7.9 Hz, 3H), 7.72 (d, J = 8.4 Hz, 1H), 7.46 (dd, J = 13.0, 7.6 Hz, 2H), 4.80 (s, 1H), 4.78–4.73 (m, 2H), 1.22 (dd, J = 6.0, 3.3 Hz, 12H). ^{13}C NMR (101 MHz, CDCl$_3$, ppm): δ 157.4, 145.7, 145.5, 137.6, 136.4, 136.3, 136.0, 133.0, 128.8, 128.4, 127.5, 126.5, 77.4, 74.2, 51.1, 33.0, 23.0, 21.8.

Synthesis of Compound B2P. A mixture of compound **4** (167 mg, 0.4 mmol) and *p*-benzoquinone (166 mg, 1.5 mmol) in 5 mL of toluene were refluxed for 1 h. After removal of the solvent, the residue was purified by column chromatography (silica gel, petroleum ether : DCM =1:1) to give **B2P** as red powders (95 mg, 57% yield). Elem. Anal. Calcd for C$_{22}$H$_{21}$N$_4$OS$_2$: C, 62.68; H, 5.02; N,

13.29; Found: C, 62.61; H, 5.06; N, 13.06. ESI-HRMS (*m/z*): calcd. for $C_{22}H_{21}N_4OS_2$, 421.1157 [M + H]$^+$; Found: 421.1153.
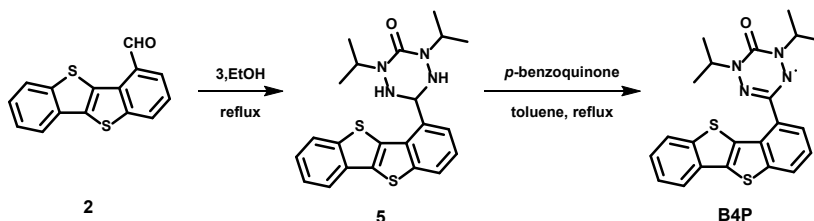
Synthesis of Compounds 5 and B4P. The Similar procedure as above gave compound **5** as white powders (yield: 37%) and **B4P** as red powders (yield: 75%). Compound **5**: ^{1}H NMR (400 MHz, CDCl$_3$, ppm): δ 7.99–7.92 (m, 3H), 7.51–7.43 (m, 4H), 5.42 (s, 1H), 4.73 (dt, *J* = 12.8, 6.3 Hz, 2H), 1.27 (d, *J* = 6.4 Hz, 6H), 1.13 (d, *J* = 6.7 Hz, 6H). ^{13}C NMR (101 MHz, CDCl$_3$, ppm): δ 158.0, 137.5, 135.3, 135.0, 133.4, 128.9, 128.4, 128.2, 127.1, 125.0, 124.4, 77.4, 73.2, 51.1, 33.0, 22.7, 22.4. **B4P**: Elem. Anal. Calcd for $C_{22}H_{21}N_4OS_2$: C, 62.68; H, 5.02; N, 13.29; Found: C, 62.68; H, 4.97; N, 13.27. EI-HRMS (*m/z*): calcd. for $C_{22}H_{21}N_4OS_2$: 421.1157 [M + H]$^+$; Found: 421.1151.
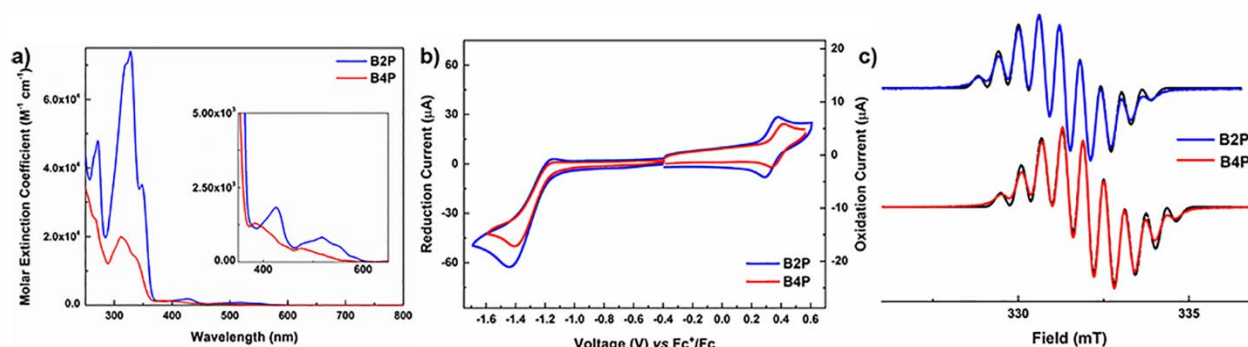
UV-*vis*, CV and EPR Measurements of B2P, B4P.

Figure S1. a) Absorption spectra of B2P and B4P in CH$_2$Cl$_2$; b) CV measurements of B2P and B4P in CH$_2$Cl$_2$; c) X-band EPR spectra of B2P and B4P in degassed d_8-toluene at 298 K, where black lines represent their simulated spectra.

EPR Parameters Fitting of B2P and B4P.

Table S1. EPR parameters of B2P and B4P.

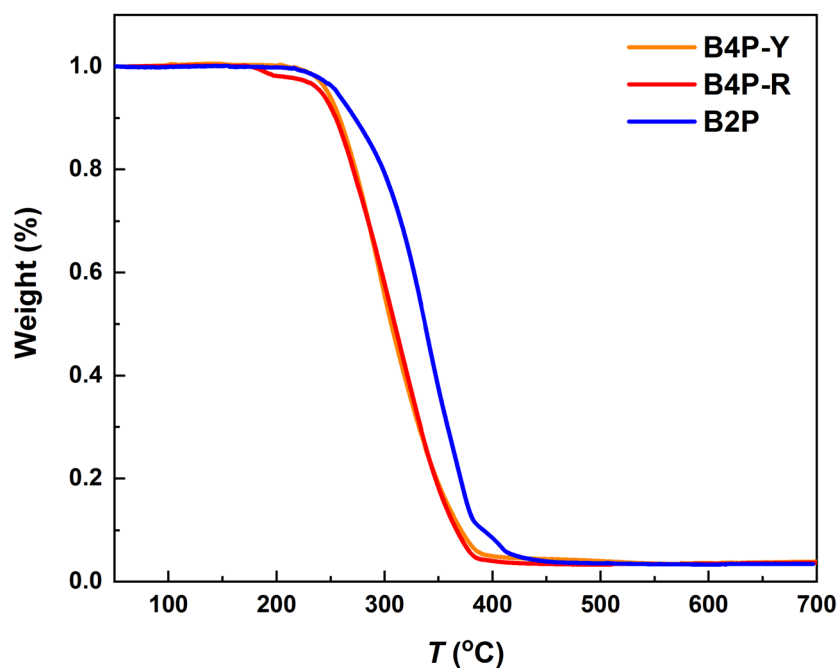|	*g* factor	A_{N1} / MHz	A_{N2} / MHz	A_H / MHz
B2P	2.0033	18.50	14.30	4.49
B4P	2.0035	18.78	14.30	3.93

Thermal Stability of B2P and B4P.

Figure S2. TGA measurement of B2P, B4P-R, and B4P-Y.
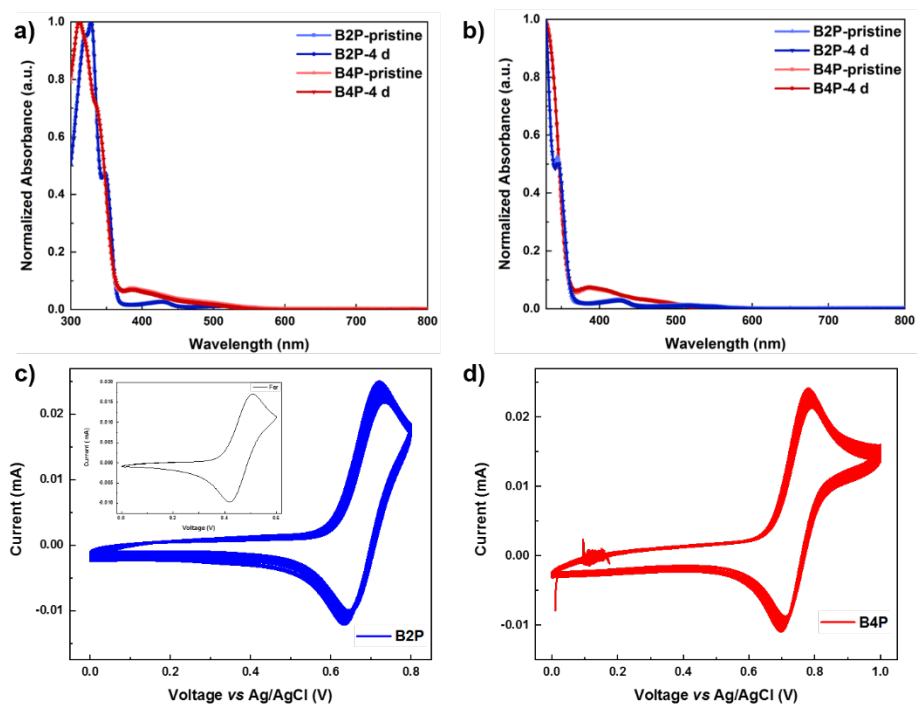
Stability Measurement of B2P and B4P.

Figure S3. a, b) Time-dependent UV-*vis* spectra of B2P and B4P under ambient conditions and in acetone containing 1% water, respectively, which reflected the stability of radicals to air. c, d) CV measurements of B2P and B4P, respectively. CV measurements were performed in CH_2Cl_2 solution

with 0.1 M *n*-Bu$_4$NPF$_6$ as electrolyte at a scan rate of 50 mV/s. The oxidation process was continuously performed 50 times in this measurement.

UV-*vis* Measurements of BTBT and Phenyl-substituted 6-Oxoverdazyl Radicals.
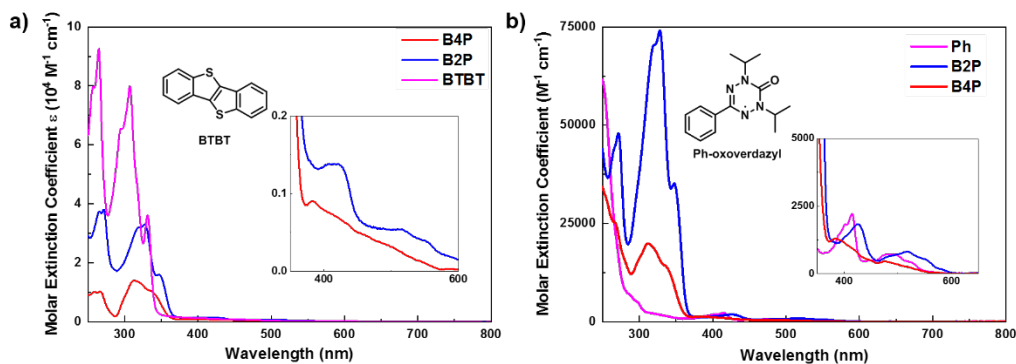
Figure S4. a) UV-*vis* spectra of BTBT, B2P and B4P in CH$_2$Cl$_2$. b) UV-*vis* spectra of phenyl-substituted 6-oxoverdazyl radical, B2P and B4P in CH$_2$Cl$_2$.

Crystal Data of B2P and B4P-R.

Table S2. Summary of crystal data for compounds B2P, B4P-R, and B4P-Y.

	B2P	B4P-R	B4P-Y
Empirical formula	C$_{22}$H$_{21}$N$_4$OS$_2$	C$_{22}$H$_{21}$N$_4$OS$_2$	C$_{22}$H$_{21}$N$_4$OS$_2$
Formula weight	421.12	421.12	421.12
Crystal system	Monoclinic	Monoclinic	Triclinic
Space group	P2$_1$/n	P2$_1$/c	P -1
a, Å	8.7493	12.5699	8.4063
b, Å	5.8992	10.2429	11.4781
c, Å	39.276	16.7280	11.8559
α, deg	90	90	78.4
β, deg	93.626	104.360	79.9

γ, deg	90	90	70.4
V, Å³	2023.1	2086.48	1048.30
Z	4	4	2
D_{calc}, g /cm³	1.384	1.342	1.335
Temperature, K	180	180.01	290

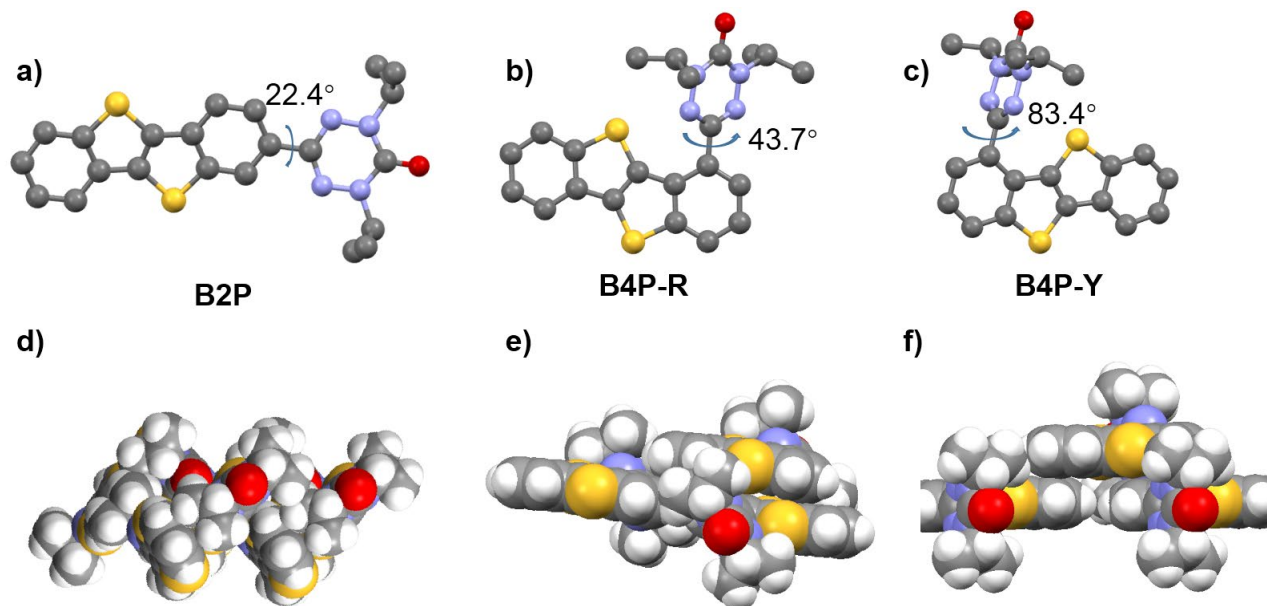**Stacking Structures of B2P, B4P-R, and B4P-Y Single Crystals.**

Figure S5. a, b, c) Molecular structures drawn by ball and stick mode of B2P, B4P-R and B4P-Y. d, e, f) Stacking structures drawn by space-fill mode of B2P, B4P-R and B4P-Y crystals.

Electrostatic Potential Computation of B2P, B4P-R, and B4P-Y.
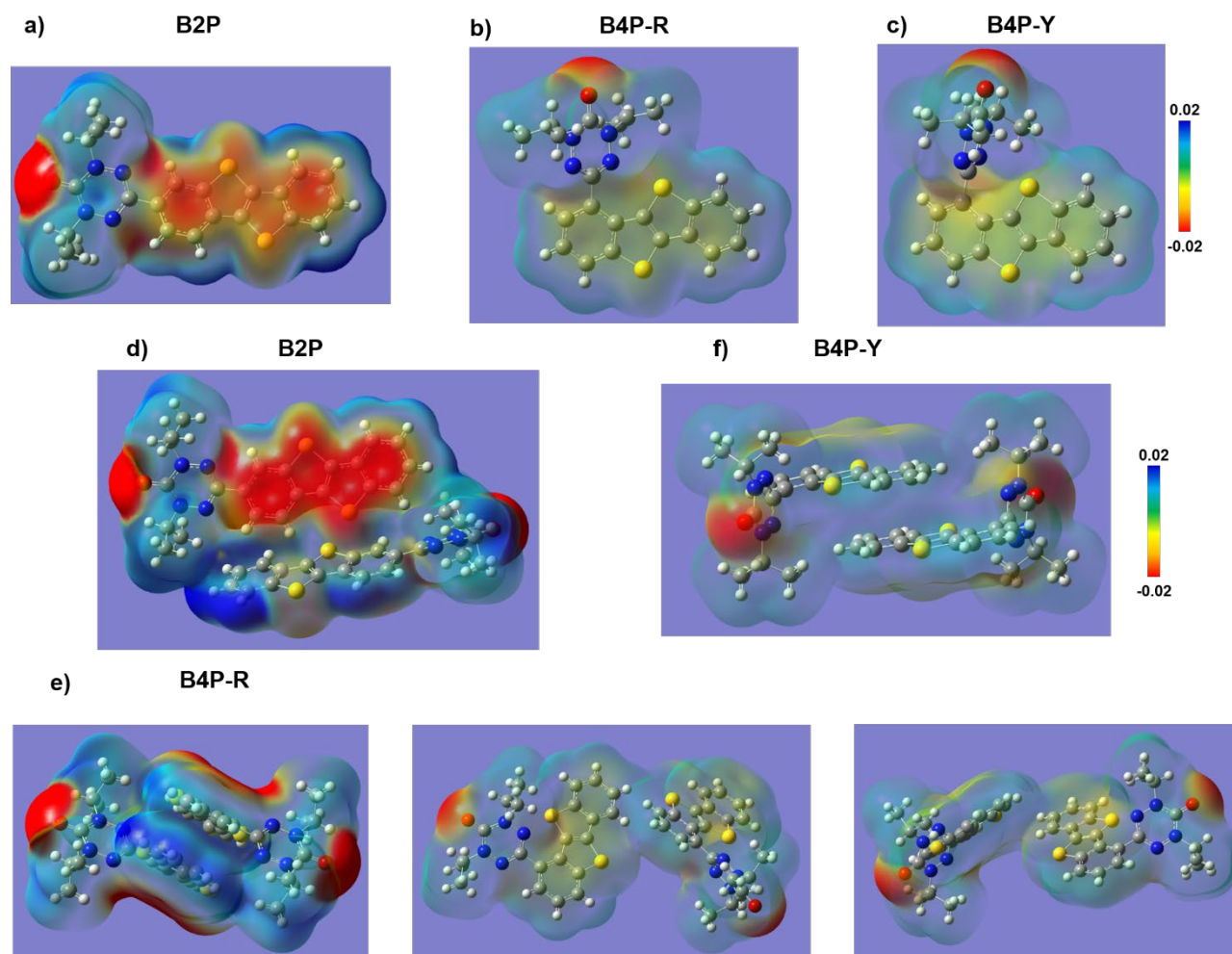
Figure S6. a, b, c) UB3LYP/6-311G(d,p)-calculated ESP maps of B2P, B4P-R and B4P-Y. d, e, f) UB3LYP/6-311G(d,p)-calculated ESP maps of B2P, B4P-R and B4P-Y dimers.

Varied-Temperature UV-*vis* Solid Absorption Spectra of B4P-Y.
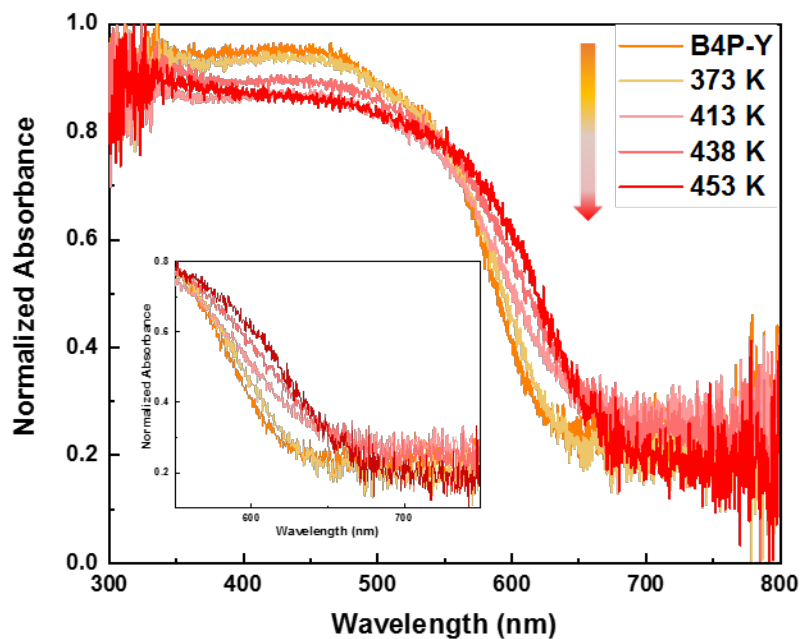
Figure S7. The absorption spectra of B4P-Y solids at various temperatures.

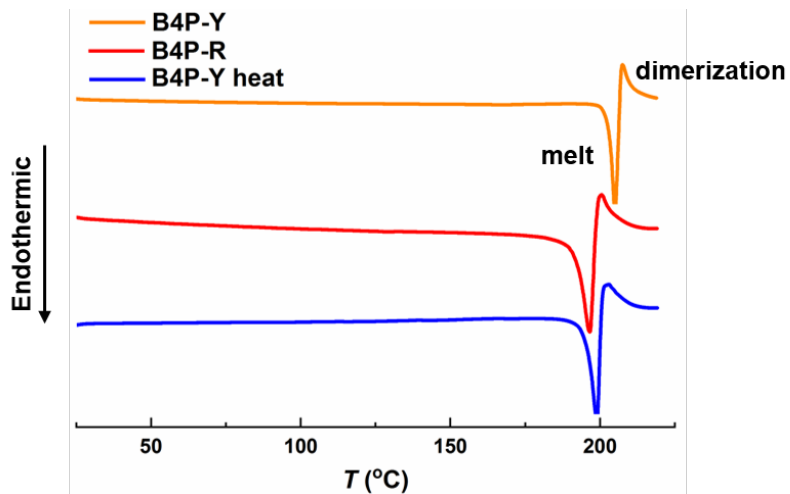**Differential Scanning Calorimetry Measurements of B4P-Y, B4P-R, and B4P-Y at ~170 ℃ for 5 minutes.**

Figure S8. Differential scanning calorimetry measurements of B4P-Y, B4P-R, and B4P-Y at ~170 ℃.

Mass Spectrum of the Solid after Heating B4P-R Single Crystals at the Melting Points for 5 Minutes.

Analysis Info

Analysis Name	FTMS-19020224_Pos_20190301_000002.d	Acquisition Date	3/1/2019 8:56:58 AM
Sample	B4P-dimer	Instrument	Bruker Solarix XR FTMS
Comment		Operator	Peking University

Meas. m/z	#	Ion Formula	Score	m/z	err [ppm]	Mean err [ppm]	mSigma	rdb	e⁻ Conf	N-Rule
843.238345	1	C44H43N8O2S4	100.00	843.238634	0.3	-1.6	53.4	36.0	even	ok
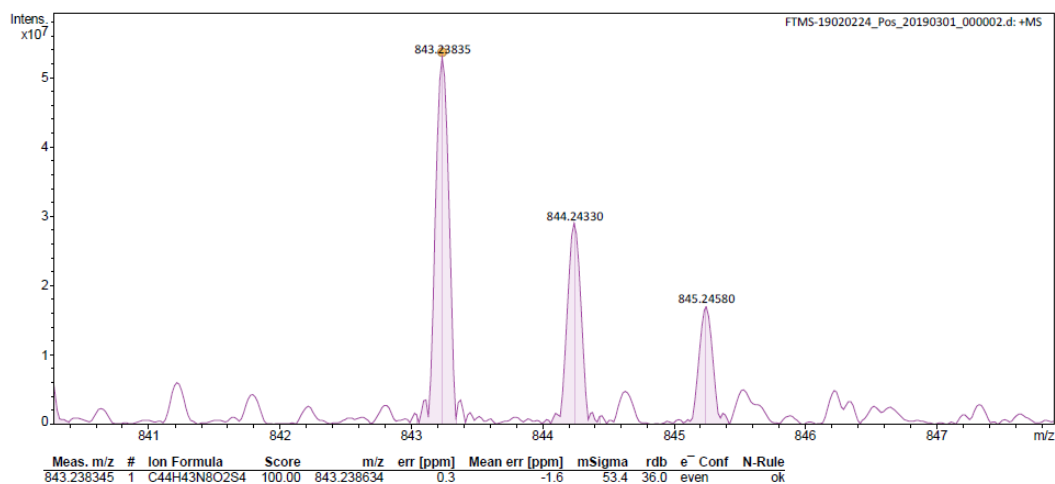
Figure S9. Mass spectrum of the solids after heating B4P-R single crystals at the melting points for 5 minutes.

DSC Measurements of B4P Crystals.
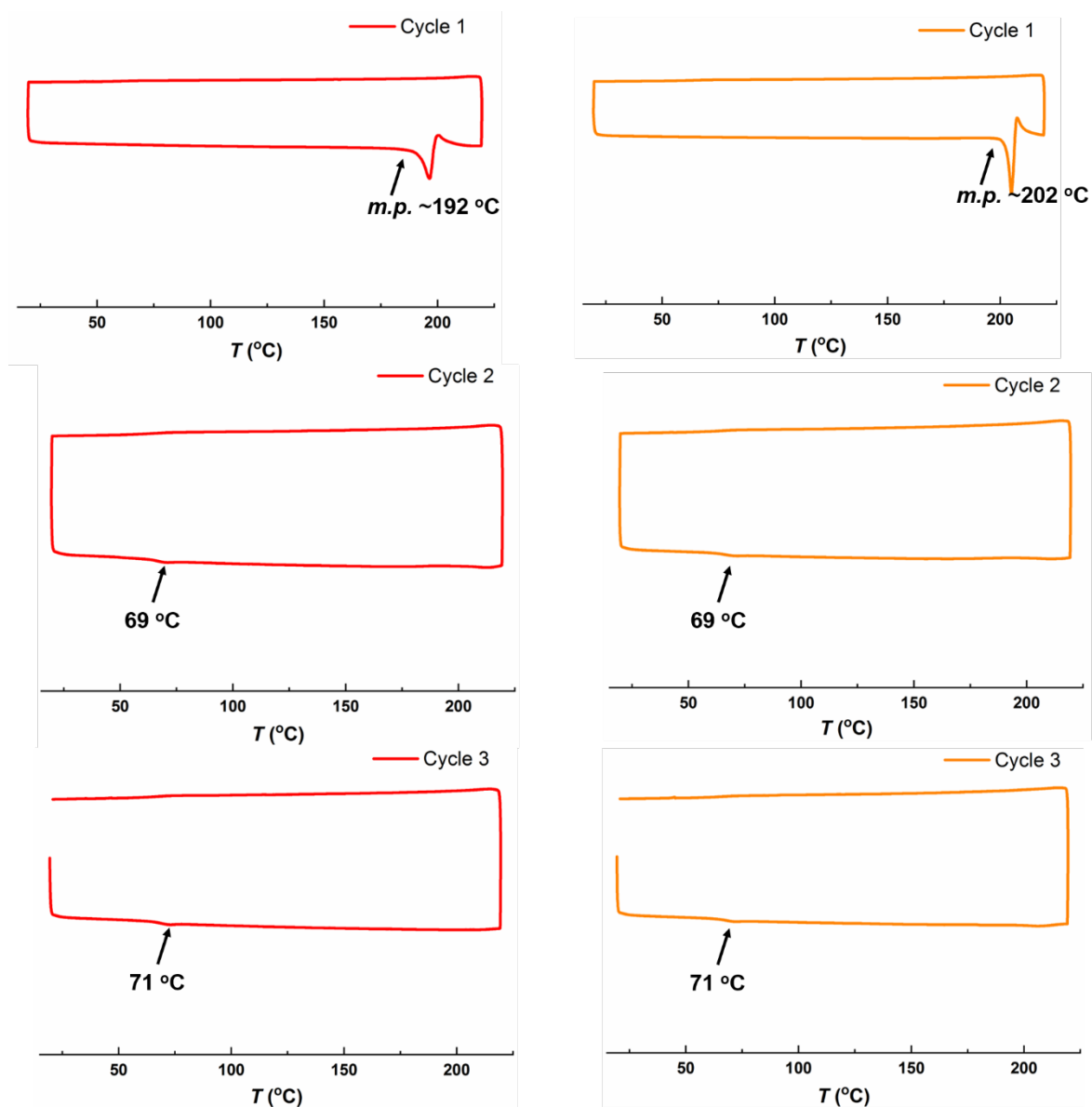
Figure S10. DSC measurements of red crystals and yellow crystals of B4P in the 1ˢᵗ, 2ⁿᵈ, 3ʳᵈ cycles, respectively.

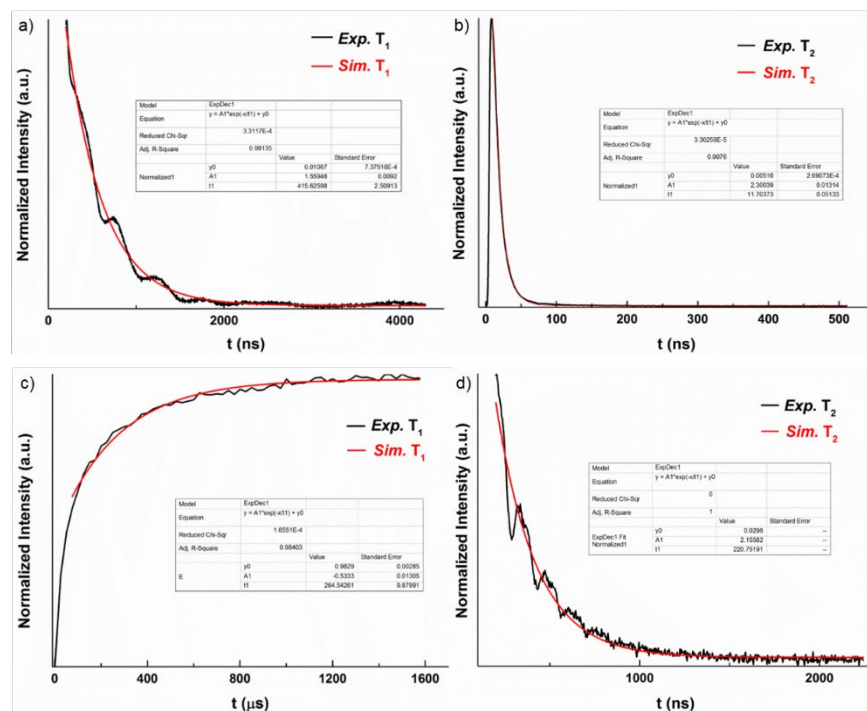**Spin-Relaxation Time Fitting of B4P-R and B4P-Y in Solid States.**

Figure S11. a, b) Spin-relaxation time of B4P-R; c, d) Spin-relaxation time of B4P-Y.
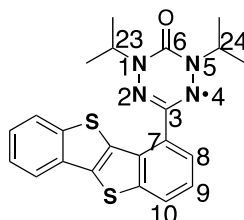
Spin Density Distribution of B4P-R and B4P-Y.

Table S3. Spin density distribution on the 6-oxoverdazyl ring and the phenyl ring of BTBT moiety calculated by DFT (broken-symmetry UB3LYP/6-31G**, the atom numbers were shown in the above molecular structure of B4P).

	B4P-R	B4P-Y
N1	0.2114	0.2102
N2	0.3769	0.3812
C3	-0.1494	-0.1605
N4	0.3758	0.3863
N5	0.2124	0.2141
C6	-0.0331	-0.033
C7	0.0211	0.0102
C8	-0.0172	-0.0061
C9	0.0087	0.0032
C10	-0.015	-0.0032
C23	-0.0123	-0.0123
C24	-0.0116	-0.0125

The spin density distribution on the C3 substituents (BTBTs in our work) is caused by the spin polarization. The single occupied molecular orbital (SOMO) of 6-oxoverdazyl radical has a node at the point of attachment to its substituent, however, the spin polarization of the next highest (doubly) occupied orbital (NHOMO) would have some influence on the final spin density. Both SOMO and NHOMO of B4P-R and B4P-Y were calculated. As shown in Figure S12, there are subtle differences in the electronic structures of two radicals. In both radicals, the four nitrogen atoms account for most spin densities in view of SOMOs, and O (C=O), C6, and C3 are the nodes of SOMOs. However, the NHOMOs show some differences, which is related to the molecular conformations. For B4P-Y, the NHOMO is localized on the BTBT unit, whereas in B4P-R, the NHOMO is partially delocalized to the 6-oxoverdazyl radical, which results in different spin polarization effect. The stronger spin polarization in B4P-R leads to more spin density distribution on BTBT unit as compared to B4P-Y.
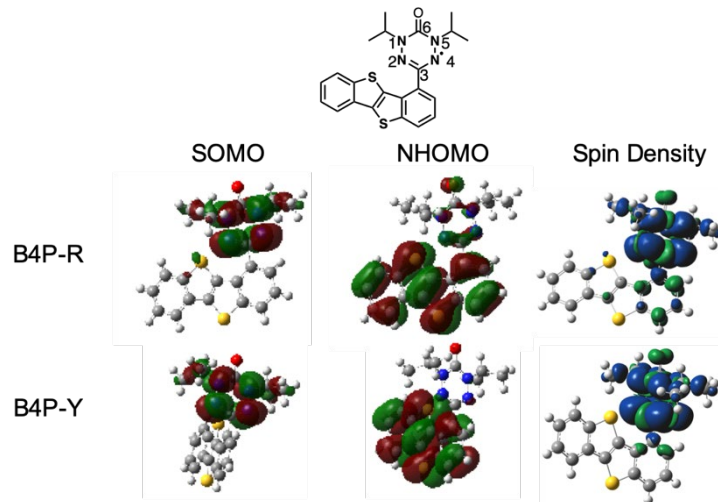

Figure S12. Single occupied molecular orbitals (SOMO), next highest (doubly) occupied orbitals (NHOMO), and spin density plots for radicals B4P-R and B4P-Y.

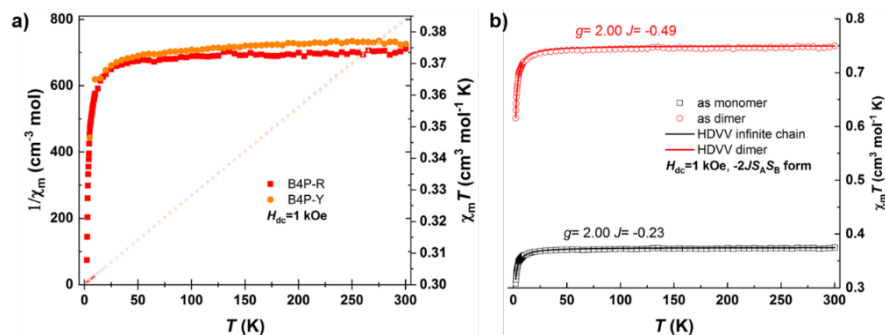**SQUID Measurements of B4P-R and B4P-Y Crystals.**

Figure S13. SQUID measurements of B4P-Y and B4P-R, in which the exchange interaction was

calculated according to $\hat{H} = 2JS_AS_B$ (the unit of exchange interaction is cm^{-1} in the graph).
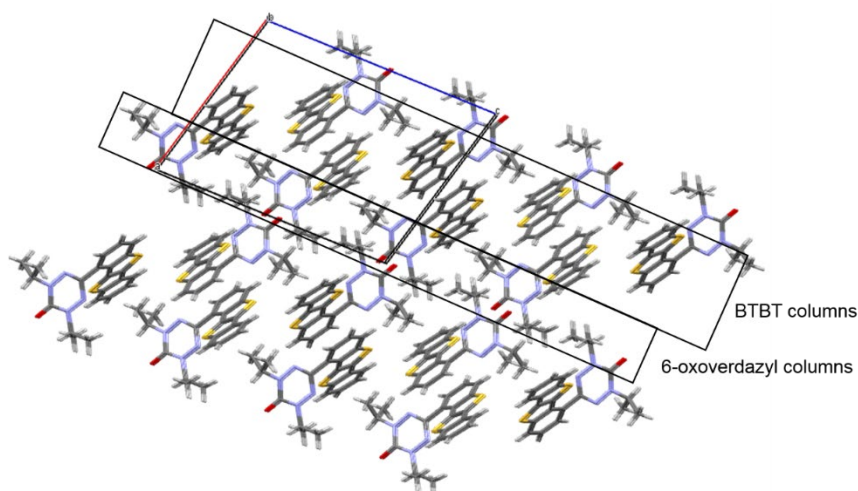
Packing Structure of B4P-R.

Figure S14. The 2D brick layer packing mode in B4P-R crystals.

EPR Measurements of B4P Single Crystals and the Proposed Dimers.

Taking B4P-Y as an example, its single crystals exhibited obvious EPR signal at room temperature. Upon heating B4P-Y to its melting point in glove box and then cooling down, the EPR signal disappeared (in Figure S15). When dissolving this EPR silent solid in d_8-toluene, the characteristic nine-line shape of EPR signal appeared again, which indicates the existence of unpaired electron and its delocalization on 6-oxoverdazyl rings. Such result demonstrated that the recovered signal was consistent B4P-Y in solution. However, the intensity of redissolved samples could not be completely reversible. One possible reason is that the dimerization accompanied with other side reactions.
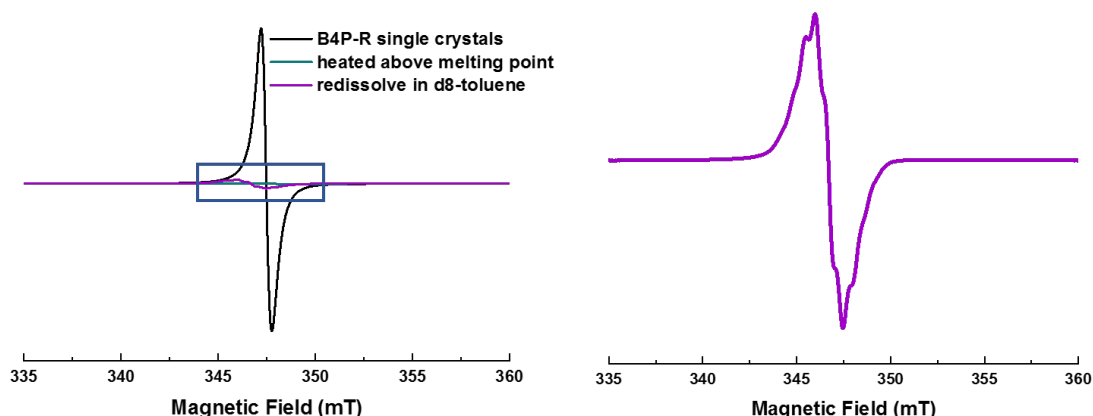
Figure S15. EPR measurements of B4P-Y single crystals, solids above melting point and redissolved in d_8-toluene (the indistinguishable line ship is due to the solution concentration is too high) at 298 K.

In-Situ Varied-Temperature Powder X-Ray Diffraction (PXRD) Measurements of B4P-Y Single Crystals.

PXRD experiments were performed to illustrate the materials that heated above melting temperature are crystalline or amorphous. Here, we only put some key temperature point in Figure S16. The diffraction pattern of B4P-Y single crystals gradually decreased and the new peak position is consistent with B4P-R single crystals (The incomplete transformation originated from the short heat time). Upon heating to 463 K, the mixture melts to a deep-red solid and displayed no diffraction peak. When cooling the temperature down to 298 K, still no diffraction peak was observed, indicating that the solid formed by heating above melting point of B4P-Y is amorphous.
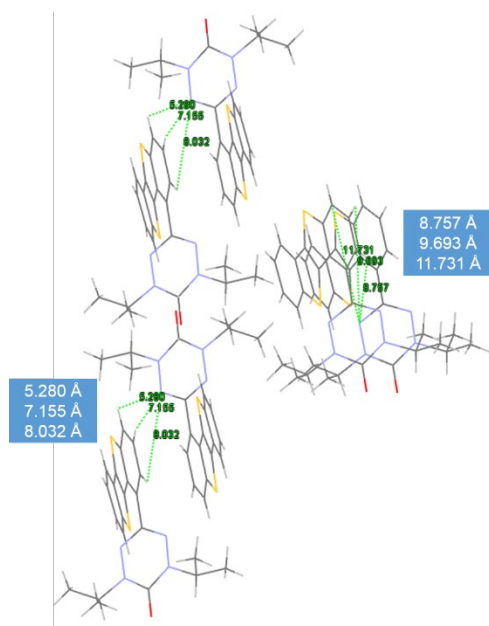
Figure S16. PXRD patterns of B4P-Y single crystals at room temperature (red line), 433 K (orange line), 463 K (blue line) and cooling to 293K (green line) and the B4P-R single crystals measured at room temperature (pink dash line).

Figure S17. Distances between nitrogen atoms in 6-oxovedazyl rings and hydrogen atoms of B4P-Y single crystals.

Figure S18. Distances between nitrogen atoms in 6-oxovedazyl rings and hydrogen atoms of B4P-R single crystals.
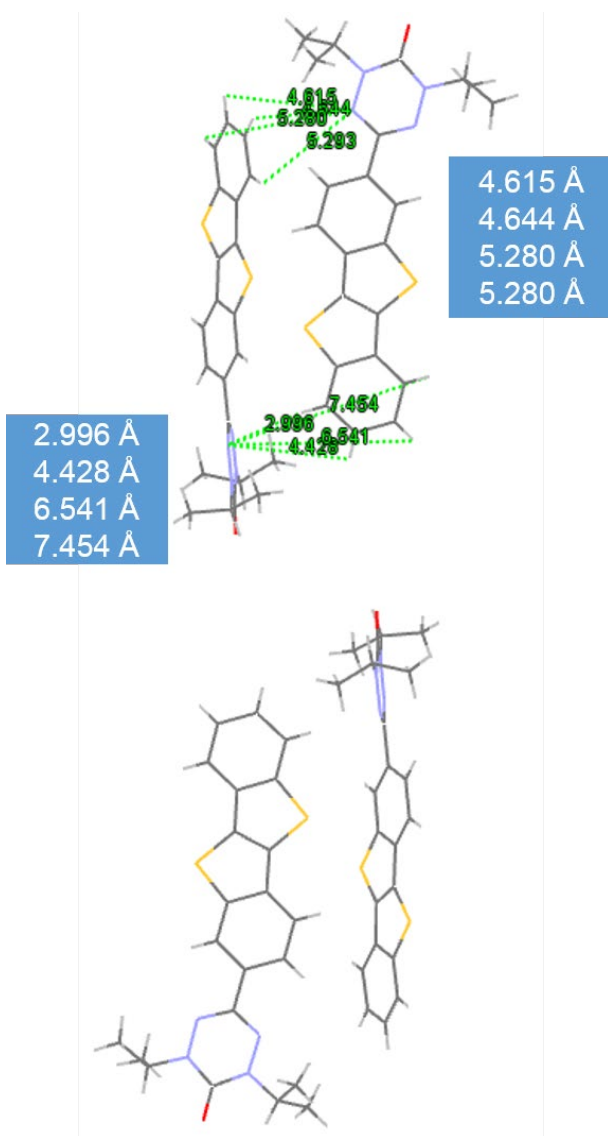
Figure S19. Distances between nitrogen atoms in 6-oxovedazyl rings and hydrogen atoms of B2P single crystals.

UV Irradiation on B4P-R and B4P-Y Single Crystals.

Table S4. Summarization of conditions and results of irradiation on B4P-R and B4P-Y single crystals.

Molecules	Irradiation Wavelength	Irradiation Power	Irradiation Time	Result
	365 nm	5%	3 hours	No reaction, still B4P-R
B4P-R	365 nm	100%	3 hours	No reaction, still B4P-R
	254 nm	-	> 3 hours	No reaction, still B4P-R
B4P-Y	365 nm	5%	3 hours	No reaction, still

			B4P-Y
365 nm	100%	3 hours	No reaction, still B4P-Y

Measurements of Spin Delocalization Values

The RDV value of B4P-R single crystal is 0.359, which is smaller than that of B4P-Y single crystal (0.365), indicating that the spin is more delocalized in B4P-R.[3] The calculated results are consistent with calculation of spin density distribution.

Table S5. RDV values of B4P-R and B4P-Y.

Single Crystals	RDV
B4P-R	0.359
B4P-Y	0.365

NMR and High-Resolution Mass Spectra of New Compounds.
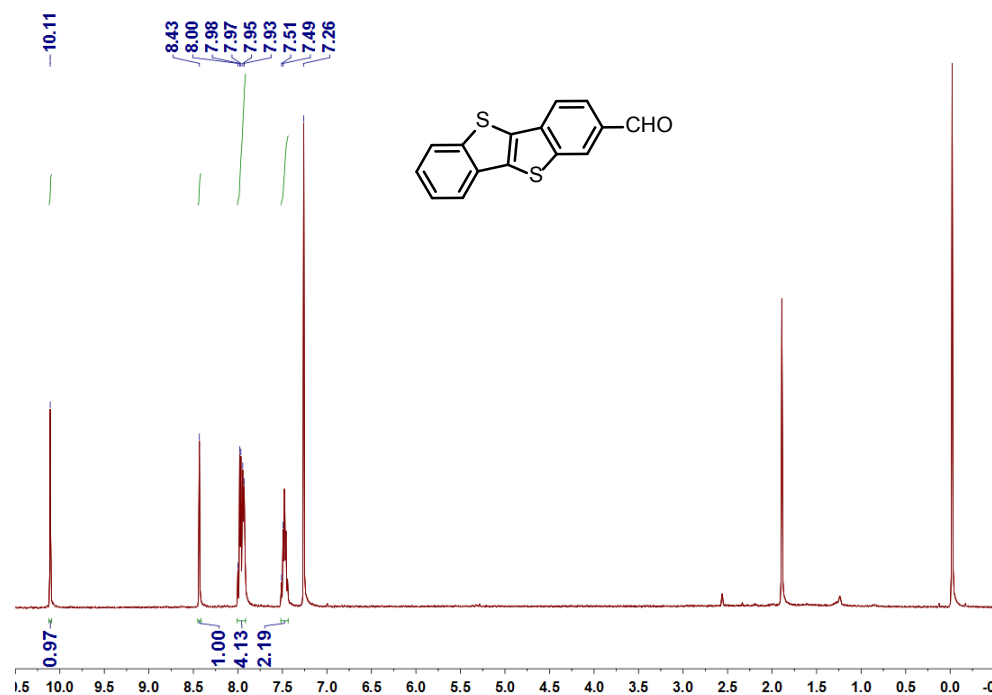
Figure S20. ^{1}H NMR spectrum of compound **1** (400 MHz, CDCl$_3$, rt).
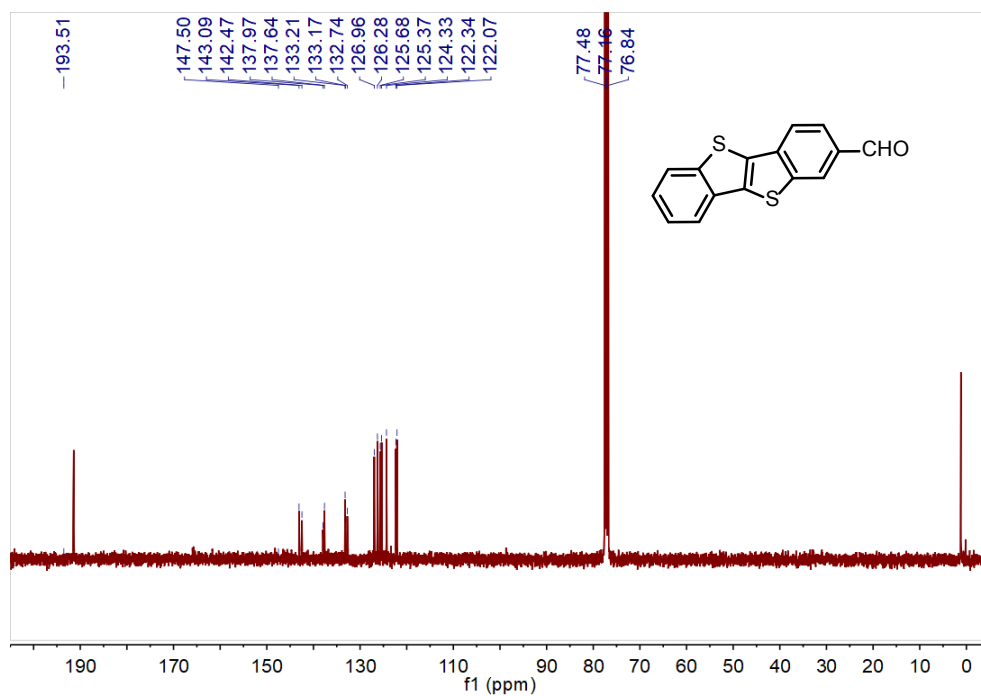
Figure S21. ^{13}C NMR spectrum of compound **1** (101 MHz, CDCl$_3$, rt).
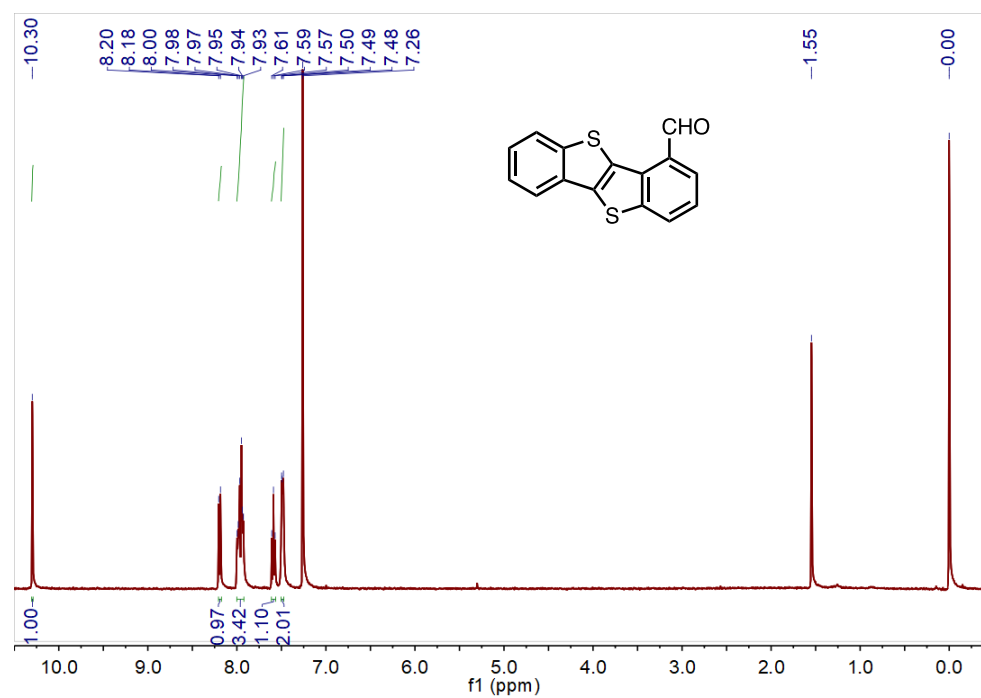
Figure S22. ^1H NMR spectrum of compound **2** (400 MHz, CDCl$_3$, rt).
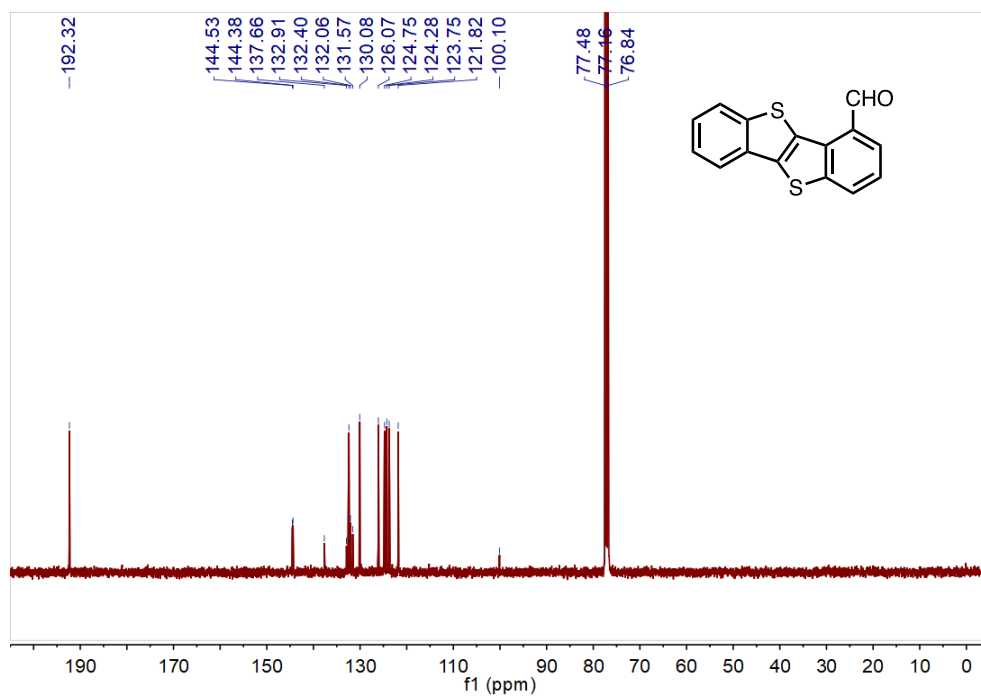
Figure S23. ^{13}C NMR spectrum of compound **2** (101 MHz, CDCl$_3$, rt).
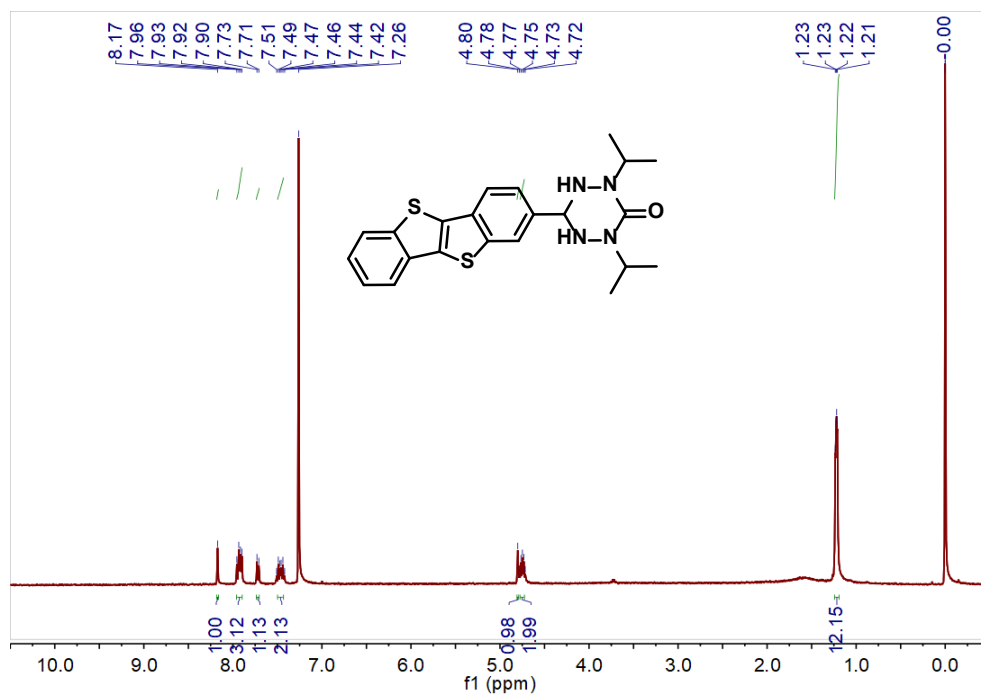
Figure S24. ^{1}H NMR spectrum of compound **4** (400 MHz, CDCl$_3$, rt).
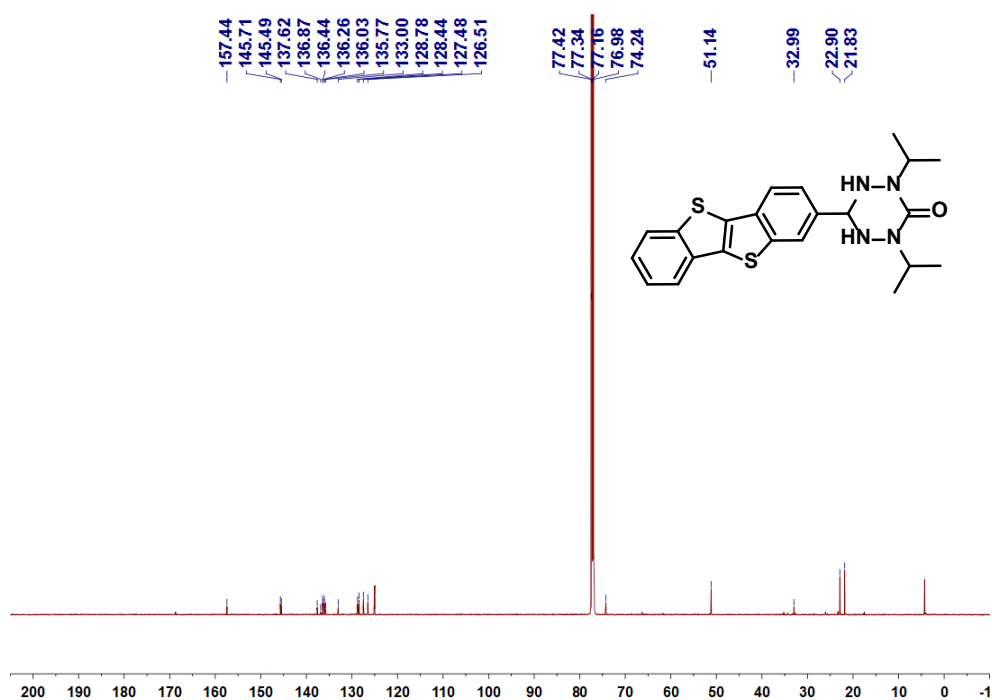
Figure S25. ^{13}C NMR spectrum of compound **4** (101 MHz, CDCl$_3$, rt).
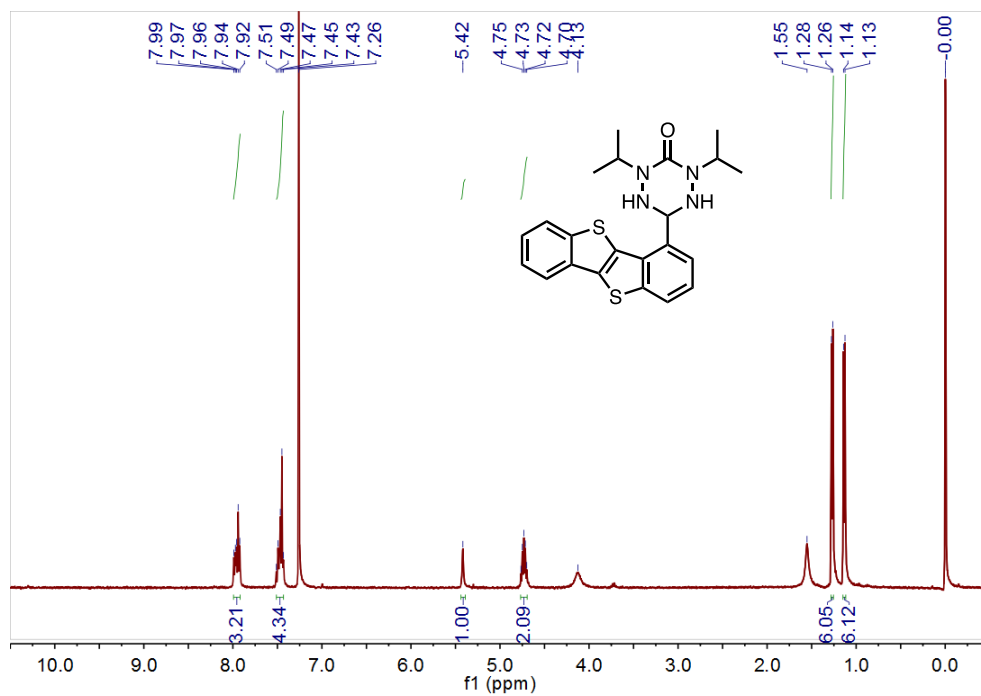
Figure S26. ^1H NMR spectrum of compound **5** (400 MHz, CDCl$_3$, rt).
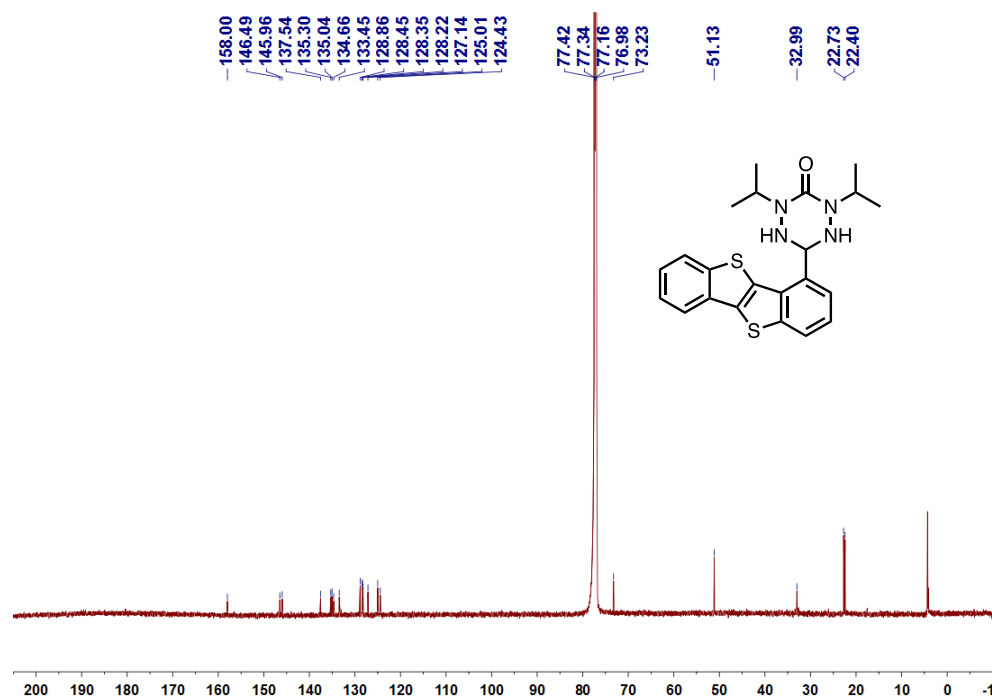
Figure S27. ^{13}C NMR spectrum of compound **5** (101 MHz, CDCl$_3$, rt).

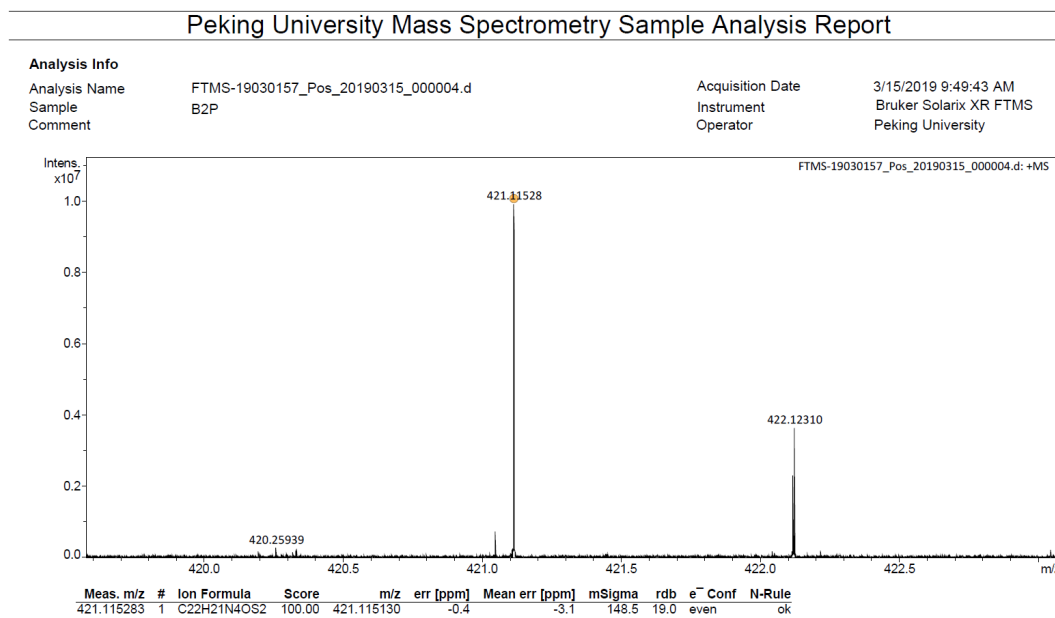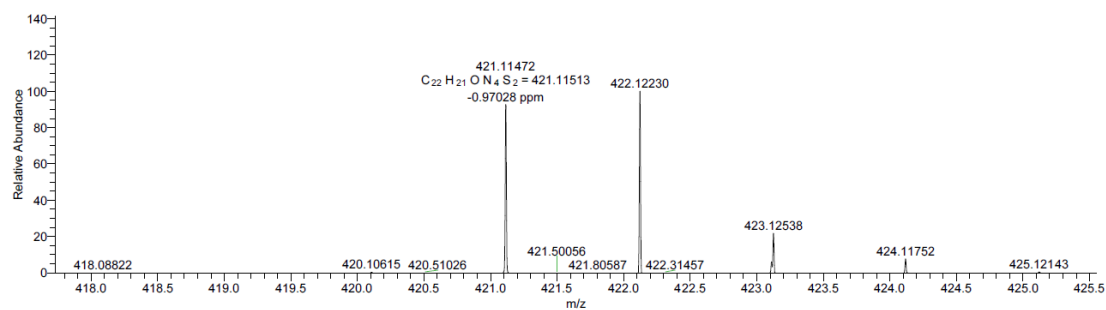**Figure S28**. HR mass spectrum (ESI) of compound **B2P**.

Figure S29. HR mass spectrum (EI) of compound **B4P**.

References:

1.   B. Košata, V. Kozmík and J. Svoboda, *Collect. Czech. Chem. Commun.*, **2002,** *67*, 645-664.

2.   E. C. Paré, D. J. R. Brook, A. Brieger, M. Badik and M. Schinke, *Org. Biomol. Chem.*, **2005,** *3*, 4258-4261.

3.   F. De Vleeschouwer, A. Chankisjijev, W. Yang, P. Geerlings and F. De Proft, *J. Org. Chem.*, **2013,** *78*, 3151-3158.